ARTICLES

Photodissociation of Propargyl Chloride at 193 nm

Laura R. McCunn, Doran I. G. Bennett, and Laurie J. Butler*,†

The James Franck Institute and Department of Chemistry, The University of Chicago, Chicago, Illinois 60637

Haiyan Fan, Fernando Aguirre, and Stephen T. Pratt

Chemistry Division, Argonne National Laboratory, Argonne, Illinois 60439

Received: May 3, 2005; In Final Form: November 14, 2005

The photodissociation of propargyl chloride (C_3H_3Cl) has been studied at 193 nm. Ion imaging experiments with state-selective detection of the Cl atoms and single-photon ionization of the C_3H_3 radicals were performed, along with measurements of the Cl + C_3H_3 and HCl + C_3H_2 recoil kinetic energy distributions, using a scattering apparatus with electron bombardment ionization detection to resolve the competing Cl and HCl elimination channels. The experiments allow the determination of the Cl ($^2P_{3/2}$) and Cl ($^2P_{1/2}$) (hereafter Cl*) branching fractions associated with the C−Cl bond fission, which are determined to be 0.5 ± 0.1 for both channels. Although prior translational spectroscopy studies by others had concluded that the low velocity signal at the Cl^+ mass was due to daughter fragments of the HCl elimination products, the present work shows that Cl atoms are produced with a bimodal recoil kinetic energy distribution. The major C−Cl bond fission channel, with a narrow recoil kinetic energy distribution peaking near 40 kcal/mol, produces both Cl and Cl*, whereas the minor (5%) channel, partitioning much less energy to relative kinetic energy, produces only ground spin−orbit state Cl atoms. The maximum internal energy of the radicals produced in the low-recoil-kinetic-energy channel is consistent with this channel producing electronically excited propargyl radicals. Finally, in contrast to previous studies, the present work determines the HCl recoil kinetic energy distribution and identifies the possible contribution to this spectrum from propargyl radicals cracking to C_3^+ ions in the mass spectrometer.

I. Introduction

The study of the near-ultraviolet photodissociation dynamics of alkyl halide molecules has a long and rich history.[1−9] Systematic studies of the product channels and branching fractions, as a function of the alkyl group, have provided substantial information on the transitions carrying the oscillator strength, the nature of the dissociative potential surfaces, and the dissociation mechanisms. For saturated radicals, the absorption spectra of alkyl halides at ∼200 nm results from the excitation of a nonbonding electron of the halogen atom to the σ^* orbital of the C−X bond.[1−3,5] The antibonding character of the σ^* orbital results in rapid C−X bond fission. For unsaturated radicals, the situation is more complex. Although the $n\sigma^*$ transition still contributes, oscillator strength in the near-ultraviolet is predominantly carried by the $\pi\pi^*_{C=C/C\equiv C}$ transition involving the π orbitals of the double or triple bond(s).[3,5,8,9] In addition, as reported by Browning et al.,[5] for lower-symmetry alkyl halides, the $\pi\pi^*$, $n\sigma^*$, and $n\pi^*$ transitions can be strongly mixed. Generally, the observation of C−X bond fission with a high-recoil-kinetic-energy distribution indicates that the $n\sigma^*$ state must have an important role somewhere along the dissociative reaction coordinate, whereas the observation of HX elimination and slow dissociation channels suggest a role for more complex evolution on the excited state potential surface, typically involving internal conversion and decomposition on the ground-state surface or intersystem crossing and dissociation in the triplet manifold. Measurements of the branching fractions for populating the X $^2P_{3/2}$ ground state and X $^2P_{1/2}$ (hereafter referenced as X*) spin−orbit excited state have proved extremely useful in elucidating the mechanism of C−X bond fission.[2] Similarly, determinations of the branching fractions for C−X bond fission versus HX elimination have provided additional insight into the dissociation process.[3−9]

The photodissociation of propargyl chloride at 193 nm has been examined in two previous studies in which time-of-flight (TOF) analysis was used to determine the translational energy distribution of the products, and electron-impact ionization with mass analysis was used to detect and identify the fragments.[8,9] Product angular distributions were also determined. The translational energy distribution for the C−Cl fission product channel, leaving the low-velocity signal at Cl^+ unfit, was also reported in a recent study of the photoionization cross section of the

† The submitted manuscript has been created by the University of Chicago as Operator of Argonne National Laboratory ("Argonne"), under Contract No. W-31-109-ENG-38 with the U.S. Department of Energy. The U.S. Government retains for itself, and others acting on its behalf, a paid-up, nonexclusive, irrevocable worldwide license in said article to reproduce, prepare derivative works, distribute copies to the public, and perform publicly and display publicly, by or on behalf of the Government.

* Author to whom correspondence should be addressed. E-mail: L-Butler@uchicago.edu.

10.1021/jp058148y CCC: $33.50
Published on Web 12/18/2005

propargyl radical.[10] This distribution was also obtained using translational spectroscopy, but vacuum ultraviolet photoionization of the products at 10−15 eV was used instead of electron-impact ionization. The results of the three studies are in reasonably good agreement. The translational energy distributions determined by monitoring $^{35}Cl^+$ showed a high-kinetic-energy component and a low-kinetic-energy component. The high kinetic energy component was assigned to C−Cl bond fission:[8,9]

$$C_3H_3Cl + h\nu \rightarrow C_3H_3 + Cl \text{ (or Cl*)} \quad (1)$$

Unfortunately, the ionization process was not selective in any of the three studies. As a result, the relative contributions of the Cl and Cl* channels could not be determined and no branching fractions were reported. The low-kinetic-energy component of the $^{35}Cl^+$ signal was assigned to HCl elimination:[8,9]

$$C_3H_3Cl + h\nu \rightarrow C_3H_2 + HCl \quad (2)$$

The appearance of this feature in the $^{35}Cl^+$ signal was explained as resulting from cracking of HCl^+ in the electron impact ionization of HCl, and Lee and Lin[9] estimated a daughter ion fragmentation fraction for Cl^+ of 0.72 for electron-impact excitation of HCl in their ionizer. More recent work by Harper et al. suggests that the branching ratio of Cl^+ to HCl^+ for electron impact ionization of HCl is closer to 0.3.[11] Using infrared absorption spectroscopy, Morter et al. have measured the quantum yield for HCl production from C_3H_3Cl at 193 nm to be 0.07 ± 0.01.[12] In their electron impact study, Kawasaki et al.[8] also noted a contribution at $m/e = 36$ (HCl^+) from C_3^+ ions produced by electron-impact induced fragmentation of C_3H_3, so did not report a recoil kinetic energy distribution for the HCl elimination channel.

In this paper, new results from translational spectroscopy and ion-imaging experiments are combined to provide additional insight into the photodissociation dynamics of propargyl chloride at 193 nm. Although the methodology of the translational spectroscopy experiments is similar to those reported previously,[8,9] particular attention here is devoted to resolving both the HCl elimination and C−Cl fission product channels and to identifying possible contributions from C_3^+ daughter fragments in the signal at HCl^+. State-selective detection of the Cl and Cl* obtained using different resonant multiphoton ionization schemes in the ion imaging experiments reveal the spin−orbit state of the Cl atom produced in the high-recoil-kinetic-energy and low-recoil-kinetic-energy C−Cl bond fission channels. Single-photon ionization is used to detect and image the C_3H_3 radical fragment. With the assumption that the photoionization cross section of C_3H_3 at 9.67 eV is independent of internal energy, comparison of the Cl, Cl*, and C_3H_3 translational energy distributions allows the determination of the Cl and Cl* branching fractions. The resulting values are compared with values determined by measuring the relative signal levels of the (2 + 1) ionization of Cl and Cl*, following an approach described previously.[13−19] The combined imaging results are also compared with the translational spectroscopy results on the C−Cl bond fission in an attempt to make an independent determination of the relative yields of Cl and Cl*. The translational spectroscopy data also allow the determination of the translational energy distribution in the HCl elimination channel.

II. Experiment

The ion-imaging and translational spectroscopy experiments have both been described previously. The ion-imaging spectrometer is a modified TOF mass spectrometer equipped with a lens suitable for velocity-map imaging.[20,21] The sample was introduced into the chamber via a room-temperature pulsed valve, and the resulting molecular beam was skimmed before entering the interaction region. Typically, the sample consisted of 3%−5% propargyl chloride in helium buffer gas, with a total backing pressure of ∼1500 Torr. An ArF excimer laser provided the 193-nm light, which was passed through a Glan-laser polarizer, apertured down and loosely focused into the interaction region. The 193-nm pulse energy was typically 10−30 μJ. A tunable, frequency-doubled dye laser provided the probe light for two-photon resonant, three-photon ionization of Cl and Cl*. This light was also passed through a Glan-laser polarizer and focused into the interaction region, using a 150-mm-focal-length lens. At higher probe−pulse energies, photodissociation by the probe laser was possible. For the images reported here, neutral density filters were used to reduce the intensity until the probe-only signal was negligible. As the images were recorded, the probe laser was repetitively scanned across the Doppler profile of the resonant two-photon transition. Generally, the polarizations of the two beams were parallel to each other and to the plane of the detector, although other polarization combinations were used in an attempt to characterize possible effects of alignment. Images of C_3H_3 were also recorded by ionizing the C_3H_3 photofragment with one photon of vacuum ultraviolet (VUV) light. For these measurements, the VUV light was generated by resonant difference frequency mixing in krypton, as has been described previously.[22] Images were recorded by gating the voltage on the detector to allow selective detection at the TOF of the ion of interest. The magnification of the imaging spectrometer and the calibration of the instrument were characterized using the photodissociation of methyl iodide. The images were reconstructed by using the BASEX program developed by Dribinski et al.[23] to yield the three-dimensional velocity and angular distributions.

To obtain data on the HCl elimination channel, and to help calibrate the branching fractions in the C−Cl fission channels, we also obtained photofragment velocity distributions using electron bombardment ionization of the photofragments. The rotatable-source, fixed-detector apparatus has been described in detail previously.[24] A gaseous mixture of 8% propargyl chloride in helium expanded through a continuous nozzle with a diameter of 0.1 mm, heated to 260 °C to eliminate clusters, and passed through two skimmers into the 10^{-6} Torr main chamber of the apparatus. The most probable speed in the number density distribution of the molecular beam was 13.9×10^4 cm/s with a spread ($\Delta v/v_{peak}$) of 17.7% calculated from the full-width at half-maximum. The propargyl chloride molecules were photodissociated by 193-nm photons at the crossing point between the laser and molecular beam, with the propagation direction of the laser perpendicular to the molecular beam, so the light was unpolarized in the molecular-beam-detector scattering plane. For the high-power-laser data, the 50 mJ output of a Lumonics PM 848 excimer laser was focused to a 1.5 mm × 3 mm spot in the interaction region, whereas for the low-power-laser data, the output of a GAM EX10F excimer laser produced ∼0.3 mJ/mm^2 in the interaction region. A small portion of the resulting photofragments scattered through the defining aperture into the detector region and were detected via 200 eV electron bombardment in an ionizer 44.2 cm from the interaction region. The resulting ions were mass-selected using a quadrupole and counted as a function of the total (neutral + ion) TOF of the photofragments from the time the pulsed light crossed the molecular beam. The fitting of the spectra included

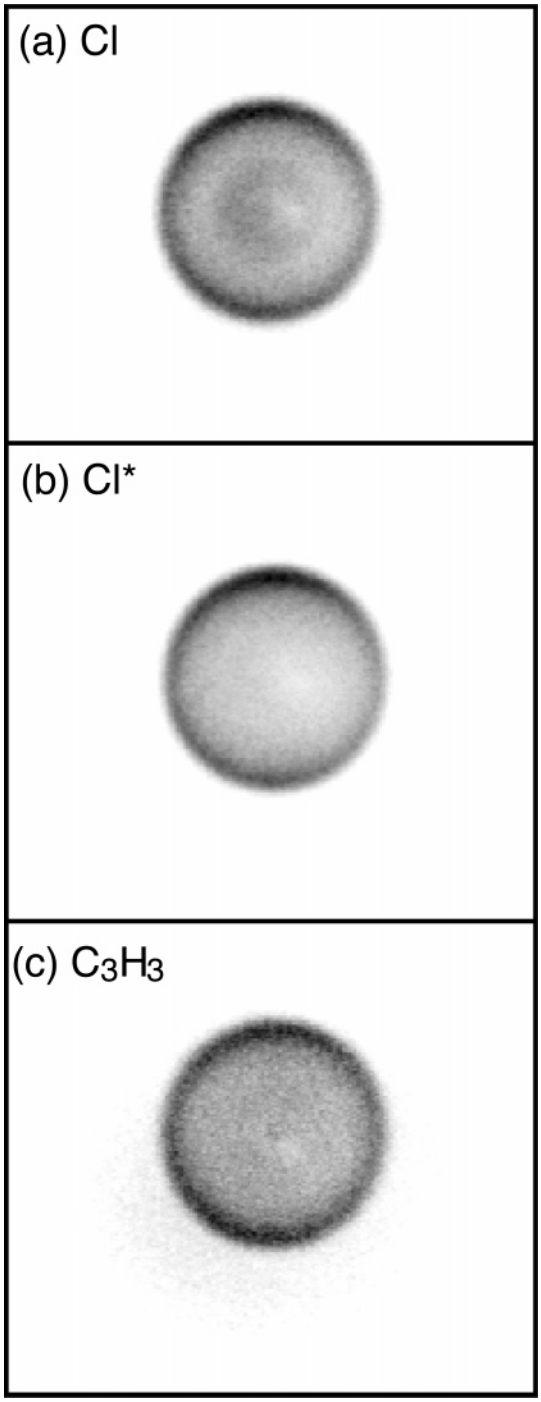

Figure 1. Images obtained by monitoring the production of Cl^+ produced by two-photon resonant, three-photon ionization of (a) Cl and (b) Cl*, and the single-photon ionization of (c) C_3H_3 following the photodissociation of propargyl chloride at 193 nm. The polarization of the photodissociation and detection lasers were parallel to each other and to the face of the detector. The polarization is oriented along the vertical axes of the images.

the separately calibrated ion transit time through the quadrupole of 4.5 μs amu$^{-1/2}$ $\sqrt{m_{ion}}$. Data were collected at m/e = 35, 36, and 39.

III. Results and Discussion

The ion images obtained following 193-nm photodissociation of propargyl chloride and monitoring the Cl, Cl*, and C_3H_3 are shown in Figure 1. The Cl and Cl* were detected by two-photon resonant, three-photon ionization via the 4p $^2D_{3/2} \leftarrow {}^2P_{3/2}$ and

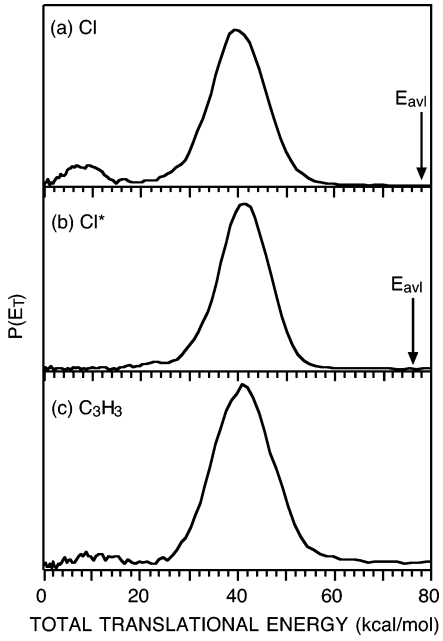

Figure 2. Total C−Cl bond fission translational energy $P(E_T)$ distributions obtained using the (a) Cl, (b) Cl*, and (c) C_3H_3 data following the reconstruction of the images shown in Figure 1. The arrows indicate the maximum allowed translational energy of 78 and 76 kcal/mol for Cl and Cl* elimination, respectively.

4p $^2P_{1/2} \leftarrow {}^2P_{1/2}$ transitions, respectively.[25] The C_3H_3 was detected by single-photon ionization at 9.67 eV. The Cl image shows two distinct features: a fast, almost-isotropic component corresponding to a large diameter ring, and a much slower, isotropic component. In contrast, the Cl* image shows only a fast, almost-isotropic ring with a slightly larger diameter than that in the Cl image. The C_3H_3 image shows characteristics intermediate between the Cl and Cl* images. Reconstruction of these images yields the three-dimensional velocity distributions. By integrating over angles and using the appropriate Jacobian, these three-dimensional distributions can be converted to $P(E_T)$ distributions of the total translational energy release. The resulting energy distributions are shown in Figure 2. The angular distribution parameters can also be extracted from the three-dimensional distributions. For linearly polarized light and the photodissociation and detection polarizations parallel to each other, the angular distribution has the following form:[26,27]

$$I(\theta) \propto 1 + \sum_i \beta_{2i} P_{2i}(\cos\theta) \qquad (3)$$

where θ is the angle between the polarization and the detection direction, β_{2i} are the angular distribution parameters, and P_{2i} are the Legendre polynomials. Generally, the sum is from i = 1 to n, where n is the total number of photons used in the photodissociation and detection steps. Alignment in the Cl $^2P_{3/2}$ M_J states can result in nonzero $\beta_{2i\geq 4}$ parameters when resonant multiphoton ionization is used for detection.[27] These additional parameters affect the physical interpretation of the β_2 parameter. For the present data, however, using terms with $i > 1$ produced no meaningful improvement in the fit, and only β_2 values were determined.

The maxima of the translational energy distributions and the angular distribution parameters are shown in Table 1, along with the corresponding values from previous measurements. As expected from the images, the Cl* translational energy distribution peaks at slightly higher energy than the Cl distribution. The energies of the fast peaks in the present distributions lie

TABLE 1: Most Probable Translational Energies and Anisotropy Parameters

	Total Translational Energy (kcal/mol)				β_2	
species	present	ref 8[a]	ref 9[a,b]	ref 10[a]	present	ref 9[a]
Cl	8 ± 1	9.0	<4.8	*c*	0.0 ± 0.1	
Cl	40 ± 2	35.0	33.4	42	0.3 ± 0.1	0.2
Cl*	41 ± 2	35.0	33.4	42.1	0.3 ± 0.1	0.2
C_3H_3	8 ± 1				0.0 ± 0.1	
C_3H_3	41 ± 2				0.4 ± 0.1	

[a] Reported values are for the combined Cl + Cl* signal. [b] The value corresponds to the average translational energy, rather than the peak of the distribution. [c] This low-energy feature was observed but not fit in the data analysis.

somewhat above those of Kawasaki et al.[8] and Lee and Lin,[9] and slightly below that of Robinson et al.[10] for the combined Cl + Cl* distributions. The small discrepancies are most likely a result of uncertainties in the calibration procedures of the different experiments. The matching of the peak positions of the Cl and Cl* distributions with those from the C_3H_3 distribution, which was obtained using a very different detection process and calibrated at a different time, provides confidence in our calibrations, which we believe are accurate to ±2 kcal/mol. The energy of the slow peak in the present Cl distribution is in good agreement with the energy of the slow peak of Kawasaki et al.,[8] but somewhat higher than the value of Lee and Lin.[9] Although Robinson et al.[10] observed a slow component in their TOF data, they did not fit it in their analysis. The Cl and Cl* angular distribution measurements are in good agreement with the previous results of Lee and Lin.[9] The imaging experiments also provide the angular distributions parameters as a function of the translational energy. However, in the present measurements, these parameters are essentially constant across a given component of the translational energy distributions. We note there is a small discrepancy between the present angular distribution parameters determined from the Cl and Cl* images and the C_3H_3 image. This discrepancy is most likely a result of the slight asymmetry of the images, as seen in Figure 1. In the Cl and Cl* images, this asymmetry is, in part, a result of uncertainties introduced in scanning over the Doppler profile of the two-photon transition. Spatial nonuniformity of the detector response in the three images, and its effect on the angular distribution parameters, may also contribute to this discrepancy.

Because the slow peak is observed in both the Cl and C_3H_3 detection channels, it can be unambiguously assigned as coming from C−Cl bond fission, and not from the cracking of HCl, as was suggested previously. Note that, in the present experiments, sequential elimination of HCl from propargyl chloride and subsequent dissociation to H + Cl is energetically forbidden, following the absorption of a single 193-nm photon. The prior work using electron bombardment detection of the photofragments attributed the low-velocity signal at $m/e = 35$ to daughter ions of the HCl elimination products and the high-velocity signal at $m/e = 36$ to C_3^+ daughter ions of propargyl radicals formed in C−Cl bond fission.[8,9] As a result, these authors reported only a high-kinetic-energy channel for C−Cl fission and only a low-kinetic-energy channel for HCl elimination. Those assignments are not supported by the observation of the low-kinetic-energy C_3H_3 and Cl $^2P_{3/2}$ fragments in the ion imaging experiments presented here. As discussed below, the present translational spectroscopy data at $m/e = 36$ show a significantly different distribution from the low-kinetic-energy Cl^+ signal attributed to HCl elimination in the Lee and Lin work, providing additional support for the present assignment of the low-kinetic-energy Cl^+ signal to Cl atoms from C−Cl bond fission. These observations make it clear that there are two channels for C−Cl bond fission at 193 nm, in addition to HCl elimination as detailed below. It is noteworthy that, as in the present example, Liu and Butler[19] observed two components in the kinetic energy distribution following the photodissociation of allyl chloride, and that the fast component was observed in both the Cl and Cl* channels, whereas the slow component was only observed in the Cl channel.

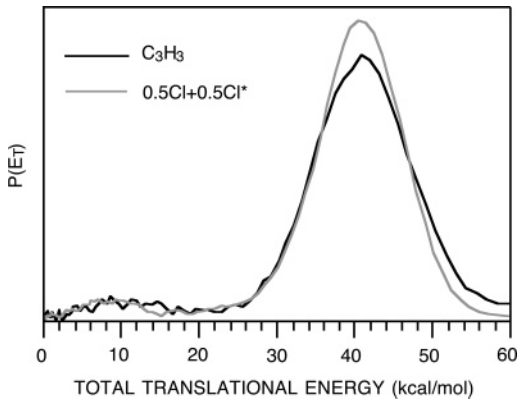

Figure 3. Comparison of the C−Cl fission $P(E_T)$ distribution determined from the C_3H_3 image with that synthesized from a 50:50 mixture of the $P(E_T)$ distributions of Cl and Cl* images. The distributions were normalized between 0 and 58 kcal/mol to eliminate the contribution from background at higher energies in the C_3H_3 distribution. The slightly poorer resolution in the C_3H_3 distribution results in a slightly reduced intensity in the high-energy peak, as compared to the synthesized spectrum.

Because the slow peak in the $P(E_T)$ distribution appears in the Cl signal and not in the Cl* signal, it is possible to use the two separate distributions to fit the C_3H_3 distribution (which should mirror the total C−Cl fission distribution producing both Cl and Cl*), and, thus, extract the Cl and Cl* branching fractions. Figure 3 shows the results of this fit for branching fractions of 0.5 ± 0.1 in both the Cl and Cl* channels. Two factors could affect the accuracy of this determination of the branching fractions. The first factor is the possibility of alignment of the Cl atoms. Because $^2P_{1/2}$ atoms cannot be aligned, the detection efficiency of the Cl* should be constant across the entire distribution in Figure 2b. In principle, however, the Cl $^2P_{3/2}$ atoms could be aligned, and the two-photon resonant, three-photon ionization efficiency could be dependent on this alignment. If the alignment shows a strong dependence on translational energy, it could, in principle, affect the analysis presented here. Hyperfine depolarization of the Cl atoms should minimize the effects of alignment.[27] In addition, images recorded for two-photon resonant, three-photon ionization via intermediate levels with $J = {}^1/_2$, ${}^3/_2$, and ${}^5/_2$ show essentially the same translational energy distributions as in Figure 2, with similar relative intensities of fast and slow components. This observation indicates that alignment of the Cl $^2P_{3/2}$ atoms is not an issue here.[28,29] The second factor that could affect the determination of branching fractions is an internal energy dependence of the photoionization cross section of the C_3H_3. For example, if, as discussed below, the slow component corresponds to an electronically excited state of C_3H_3, it could have a significantly different photoionization cross section at 9.67 eV, and, thus, the relative intensities of the two components in the C_3H_3 distribution would not reflect their true intensities. As a result, an alternative determination of the Cl and Cl* branching fractions is desirable.

As described previously, an alternate approach to determining the Cl/Cl* branching fractions is to measure their relative intensities following two-photon resonant, three-photon (2 + 1) ionization and correct the observed intensities, using experimentally determined relative line strengths. The Cl/Cl* ratio is particularly amenable to this approach, because the corresponding (2 + 1) transitions are very close to each other, minimizing corrections for different laser intensities, and because the line-strength factors for these transitions have been measured previously.[13−19] The relative line strengths for the $^2D_{3/2} \leftarrow {}^2P_{3/2}$ and $^2P_{1/2} \leftarrow {}^2P_{1/2}$ two-photon transitions used here were determined using the known Cl/Cl* branching fractions for the photodissociation of HCl at 193 nm. Unfortunately, there is some disagreement over the values of these branching fractions, yielding ratios of the $^2P_{3/2}$ and $^2P_{1/2}$ line strengths of 0.85 ± 0.10 and 0.60.[13−17] It is also possible that differences in the alignment of the Cl $^2P_{3/2}$ produced by the photodissociation of HCl and C_3H_3Cl could affect the relative line strengths, to a small degree.[30,31] Nevertheless, applying this approach to the Cl and Cl* yields from propargyl chloride at 193 nm yields branching fractions of 0.55 Cl to 0.45 Cl* and 0.64 Cl to 0.36 Cl* for line-strength ratios of 0.85 and 0.6, respectively. Quantification of the error bars for this approach is rather difficult; however, the counting statistics alone result in an uncertainty of ±0.03 in the branching fractions. Both results are in reasonable agreement with the values determined from the Cl, Cl*, and C_3H_3 images, suggesting that the photoionization cross section of C_3H_3 is not strongly dependent on internal energy.

Although the two determinations of the Cl and Cl* branching fractions are in agreement, each has potential drawbacks, and it would be desirable to confirm the values by a third independent determination. For this reason, translational spectroscopy with electron impact ionization was used to determine the TOF distribution of the total Cl atom signal, with the goal of fitting this distribution with the appropriate weightings of the independent Cl and Cl* distributions from the imaging experiments. Although it was initially believed that this determination would provide an independent test of the branching fractions, for the reasons discussed below, it was ultimately discovered that the results of this approach are inconclusive.

Figure 4a shows our new TOF data for $m/e = 35$ (Cl^+) at relatively high photolysis pulse energies, whereas Figure 4b shows the same data at significantly lower pulse energies. Both distributions were obtained by averaging for 500 000 laser shots. The two distributions are quite similar, but the former shows additional signal on the high-energy side of the fast peak arising from a multiphoton dissociation process. Translational spectroscopy data were also collected at $m/e = 39$ ($C_3H_3^+$) for the C_3H_3 fragment produced by C−Cl bond fission; these data are very similar to, but have a lower signal-to-noise ratio than, those reported previously by Robinson et al.,[10] so they are not presented here. However, note that, although the low-velocity signal was unfit in the paper by Robinson et al.,[10] it appears clearly in both their Cl^+ and the $C_3H_3^+$ data. Lee and Lin[9] stated that no slow signal appeared in their $m/e = 39$ spectrum, and they used that information to support their conclusions that the slow signal at Cl^+ was due to daughter fragments of HCl and not to Cl products. The higher signal-to-noise data of Robinson et al.[10] provided clear evidence of a low-velocity signal at $m/e = 39$.

It is known that electron impact ionization of HCl can result in cracking to produce Cl^+, and Kawasaki et al. and Lee and Lin suggested that this process could contribute to the signal at Cl^+ and affect the resulting $P(E_T)$ distribution determined by translational spectroscopy. Indeed, Lee and Lin attributed all

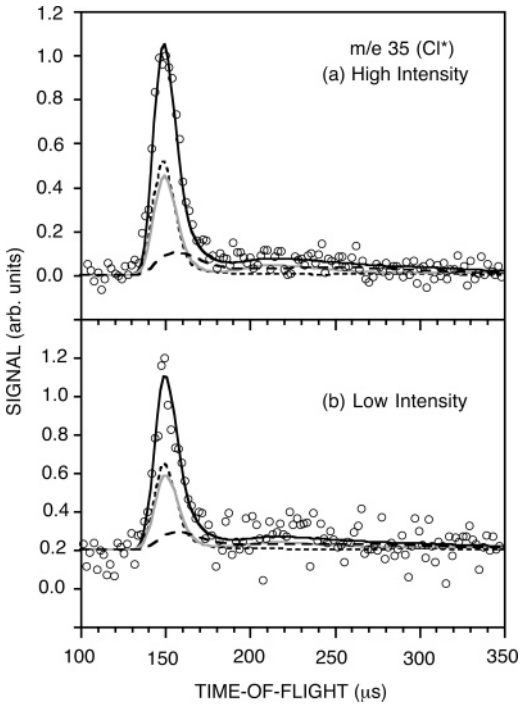

Figure 4. Time-of-flight (TOF) data collected at $m/e = 35$ (Cl^+) and a scattering angle of 10°: (a) high-intensity data collected with a laser fluence of ∼10 mJ/mm², and (b) low-intensity data collected with a fluence of ∼0.3 mJ/mm². The signal corresponds to Cl atoms from C−Cl bond fission and Cl^+ daughter ions from the HCl elimination products upon 193-nm photodissociation of propargyl chloride. The solid line corresponds to the fit obtained using a 50:50:20 ratio of the Cl and Cl* distributions obtained from the imaging data and the HCl distribution obtained from forward convolution fitting of the $m/e = 36$ data shown in the top frame of Figure 5, respectively. The short dashed line (- - -), solid gray line, and long dashed line (− − −) correspond to the individual contributions of Cl*, Cl, and HCl cracking, respectively.

the low-kinetic-energy signal at Cl^+ to daughter ions of HCl photofragments. For this reason, the detailed shape of the HCl $P(E_T)$ curve is important for fitting the signal at Cl^+ and determining the C−Cl bond fission (producing both Cl and Cl*) $P(E_T)$ distribution. Figure 5 shows the present translational spectroscopy data collected at $m/e = 36$ (HCl^+, C_3^+), corresponding to the signal from elimination of HCl and from daughter fragmentation of propargyl radicals in the electron bombardment ionizer. This distribution was recorded by averaging for 2 750 000 laser shots, that is, 5.5 times longer than that for the corresponding Cl^+ data. Note there is a fast shoulder at very fast arrival times in these data that is due to two-photon dissociation, similar to the shoulder in the high-laser-power Cl^+ signal, so we leave that as unfit. The two frames of Figure 5 show two limiting fits to the data; the top frame assumes that all the signal is from HCl photofragments, so it assumes that the fragmentation of propargyl radicals to $m/e = 36$ (C_3^+) in the ionizer does not contribute to the signal. The recoil kinetic energy distribution derived from that forward convolution fit is shown as a solid line in Figure 6. The lower frame of Figure 5 shows a fit assuming the maximum possible contribution to the signal from C_3^+ that is due to the dissociative ionization of propargyl radicals in the electron bombardment ionizer. This potential signal from daughter cracking is calculated from the Cl + C_3H_3 $P(E_T)$ in Figure 3, derived from the C_3H_3 imaging data. Fitting the leftover signal to HCl photofragments gives the recoil kinetic energy distribution, which is shown as a dashed line in Figure 6. Either limiting case results in a bimodal recoil kinetic energy

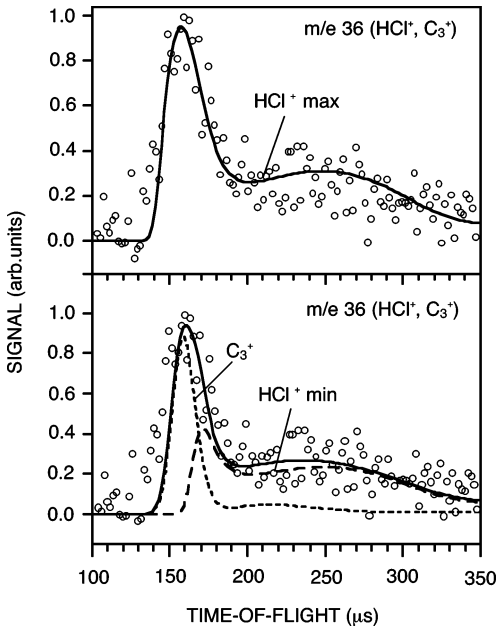

Figure 5. TOF data collected at a scattering angle of 10° and m/e = 36 (HCl^+, C_3^+). The top frame shows a fit assuming that dissociative ionization of propargyl radicals to C_3^+ does not contribute to the signal. The fit shown for the HCl^+ signal is calculated from the HCl elimination $P(E_T)$ shown in solid line in Figure 6. The bottom frame shows a fit that attributes the maximum possible amount of the signal to dissociative ionization of propargyl radicals to C_3^+ (short-dashed line fit (- - -), calculated from the C−Cl fission $P(E_T)$ derived from the C_3H_3 product shown in Figure 3). The leftover signal attributed to HCl elimination is fit using the unshaded portion of the $P(E_T)$ in Figure 6, with the resulting fit shown as the long-dashed line (− − −).

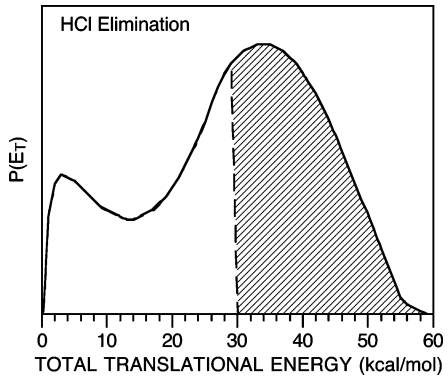

Figure 6. Translational energy distribution for the HCl elimination channel obtained from forward convolution fitting of the TOF data in Figure 5. The solid line $P(E_T)$ is derived assuming none of the signal is due to dissociative ionization of propargyl radicals to C_3^+; it gives the fit to the data shown in the top frame of Figure 5. The unshaded portion of the $P(E_T)$ is obtained by fitting the remaining portion of the signal in the m/e = 36 spectrum in Figure 5 if one attributes as much as possible of the fast signal to C_3^+ daughter ions of propargyl radicals, leaving only the low-recoil-kinetic-energy signal to HCl photofragments.

distribution for HCl elimination, similar to that in the haloalkenes studied previously; the true $P(E_T)$ for HCl elimination is somewhere between these two limits, so we show the uncertain area of the $P(E_T)$ by the shaded portion in Figure 6. Either limiting $P(E_T)$ can be used in conjunction with the C−Cl fission $P(E_T)$ to fit the data at m/e = 35. Although Figure 4 shows the fit with the HCl elimination $P(E_T)$, which is shown as a solid line, fitting the contribution to the m/e = 35 signal from daughter fragmentation of HCl photofragments with the dashed line $P(E_T)$ in Figure 6 (unshaded region) also gives a good fit with a reduced contribution from HCl daughter ions, because both give signal in the region between the small slow peak and the fast main peak, which is the region underfit by the Cl atoms from C−Cl fission. Thus, although the prior work on this system was correct in assuming there could be contamination in the m/e = 36 data by C_3^+ ions produced by dissociative electron-impact ionization of C_3H_3, Lee and Lin incorrectly assigned all the low-recoil-kinetic-energy signal at HCl^+ and Cl^+ to HCl elimination and all the high-velocity signal at Cl^+ to C−Cl fission. This work shows that the HCl elimination $P(E_T)$ is bimodal and does not account for all of the low-recoil-velocity signal at Cl^+. The fits of the m/e = 35 TOF show that much of that signal is due to a C−Cl fission channel that was also detected in the imaging data presented in this paper.

With the $P(E_T)$ distributions of Cl and Cl* from the imaging data, and the $P(E_T)$ distribution of HCl from translational spectroscopy, it should be possible to fit the total m/e = 35 $P(E_T)$ distribution from translational spectroscopy to yield the relative contributions from the Cl and Cl* channels and HCl cracking. Unfortunately, the distributions are similar enough that the m/e = 35 data can be fit by a wide range of Cl and Cl* branching fractions simply by varying the relative contribution of HCl cracking. Without a knowledge of the primary branching fractions for C−Cl bond fission, this determination is inconclusive. Figure 5 shows the results obtained using the Cl:Cl* branching fraction of 0.5:0.5 determined previously, which requires a contribution of 0.2 of Cl^+ from HCl cracking to fit the data if we assume that none of the signal at m/e = 36 is due to C_3^+ daughter fragments of propargyl radical. If we use the HCl elimination $P(E_T)$ derived from the fit to the m/e = 36 signal in the lower frame, we can fit the m/e = 35 data well with the Cl:Cl* branching fraction of 0.5:0.5 determined previously and a contribution of 0.12 from HCl cracking to Cl^+. Thus, HCl elimination has a smaller, but non-negligible, yield, compared to C−Cl bond fission; estimating this yield from the fits requires knowledge of the daughter cracking patterns of HCl upon electron bombardment ionization. We attempt this analysis in the next paragraph.

These data offer two ways to determine the branching fractions for C−Cl bond fission and HCl elimination from the photodissociation of propargyl chloride. The first method uses the ratio between the portion of the integrated signal at m/e = 36 attributed to HCl elimination and the portion of the signal at Cl^+ assigned to Cl atoms from C−Cl fission in Figures 5 and 4, respectively. To calculate the branching ratio R, we correct these relative signals for the kinematic factors in the scattering of the photofragments and the appropriate Jacobians and velocity-dependent ionization probability, using the $P(E_T)$s determined in this paper to calculate an expected signal (if the HCl elimination:C−Cl fission ratio were 1:1) at each mass in the same time interval as the data was integrated. These expected signals do not account for the ratio of ionization cross sections (σ_{ion}) and daughter cracking patterns of the fragments to the ion mass spectrum being integrated, so we also include that correction, obtaining the relation

$$R = \frac{\sigma_{Cl+C_3H_3}}{\sigma_{HCl+C_3H_2}} = \frac{Cl^+ \text{ signal}}{HCl^+ \text{ signal}} \times \frac{\text{expected signal (HCl)}}{\text{expected signal (Cl)}} \times \frac{\sigma_{ion}(HCl)}{\sigma_{ion}(Cl)} \times \frac{f_{HCl^+/HCl}}{f_{Cl^+/Cl}} \quad (4)$$

We took the m/e = 36 data used for this analysis on a different day than the m/e = 35 data and with a slightly different quadrupole resolution (and for 5.5 times as many laser shots);

however, beam velocity measurements on each day showed very similar signals (only ~10% smaller on the day we took the $m/e = 36$ data). The branching ratio obtained using the fit shown in the upper frame of Figure 5, which assumes that C_3^+ daughter ions do not contribute to the signal, is thus calculated from eq 4 as follows:

$$R = \frac{\sigma_{Cl+C_3H_3}}{\sigma_{HCl+C_3H_2}} = \frac{25783}{41632/5.5} \times \frac{95.14}{88.13} \times \frac{42.7}{35.2} \times \frac{0.613}{1} = 2.73 \quad (5)$$

Here, we have estimated the ratio of ionization cross sections for Cl and HCl (±20%) using the empirical relationship between molecular polarizability and electron bombardment ionization cross section proposed by Center and Mandl,[32] with the molecular polarizability estimated as the sum of the atomic polarizabilities.[33] We have also calculated the daughter cracking fraction of HCl to HCl^+ of 0.6127 from the data in ref 11. The expected signal ratio, assuming equal branching to each channel, was integrated over the same TOF range as the actual signal was integrated (144−200 μs for the HCl signal at HCl^+ and 124−170 μs for the Cl signal at Cl^+). Thus, assuming that there is no contribution from daughter fragments of propargyl radicals in the $m/e = 36$ data, we calculate a branching fraction of 73% C−Cl fission and 27% HCl elimination from our signal intensities attributed to each process in the $m/e = 36$ and $m/e = 35$ spectrum fits. If, instead, we attribute the maximum possible signal to C_3^+ daughter fragments in the $m/e = 36$ data, as shown in the bottom frame of Figure 5, thus attributing less signal to HCl elimination in both spectra and more signal to C−Cl fission in the $m/e = 35$ spectrum, (integrating the HCl signal under a fit, calculated from the dashed-line unshaded portion of the $P(E_T)$ in Figure 6, from 154 μs to 200 μs and the Cl signal in the $m/e = 35$ spectrum from 124 μs to 170 μs) the same branching ratio analysis gives

$$R = \frac{\sigma_{Cl+C_3H_3}}{\sigma_{HCl+C_3H_2}} = \frac{28110}{14738/5.5} \times \frac{95.14}{81.82} \times \frac{42.7}{35.2} \times \frac{0.613}{1} = 9.1$$

Thus, even if we attribute the maximum amount of the $m/e = 36$ signal to C_3^+, we still estimate a 10% branching fraction for HCl elimination. (The HCl elimination quantum yield was previously determined to be 0.07 ± 0.01.[12]) Thus, our data suggest that HCl elimination is a significant channel in the 193-nm photodissociation of propargyl chloride, with a branching fraction between ~10% and 30%. Interestingly, if one simply uses the relative contributions of C−Cl fission and HCl elimination that fitting the $m/e = 35$ spectrum required [1:0.2 or 1:0.12, depending on which limiting $P(E_T)$ for HCl elimination is used], and corrects for the daughter ion cracking fraction of HCl to Cl^+ of 0.1838 obtained in ref 11, one obtains a larger predicted branching fraction to HCl elimination. However, the HCl produced by molecular elimination is highly vibrationally excited. Thus, this discrepancy could be resolved if the electron-impact fragmentation of vibrationally hot HCl is more efficient than for cold HCl, which was measured in ref 11.

Two assumptions have been made for this analysis. The first is that the angular distribution of the HCl photofragments is isotropic. [With an unpolarized laser, the relative scaling between channels with different anisotropies must be corrected by factors of $(1 + \beta/4)^{-1}$ to account for the fact that photofragments with a parallel angular distribution are more likely to be scattered in the detector plane.] The second assumption is that the electron impact ionization probabilities of Cl and Cl* are equal, for which there is considerable support in the literature.[34]

The high-recoil-kinetic-energy Cl and Cl* peaks dominate the translational energy distributions in both the imaging and translational spectroscopy data. The Cl and Cl* branching fractions reflect the mixed character of the optically excited and dissociating states. The results do not reveal whether the mixed branching fractions result from the simultaneous excitation of two or more different electronic states, followed by dissociation on noninteracting surfaces, or if they result from the excitation of a single state carrying essentially all of the oscillator strength, followed by interactions with other surfaces on the way to dissociation. The relatively small anisotropy observed in the angular distributions does not fully resolve this issue, but the similarity of the angular distributions in the Cl and Cl* channels suggests that these products result from excitation of the same electronic state(s). Browning et al.[5] have argued previously that the emission spectra obtained for dissociating propargyl chloride following excitation at 199 nm suggest excitation of a state with mixed $\pi\pi^*$, $n\sigma^*$, and $\pi\sigma^*$ character, which is consistent with the present results. The high recoil kinetic energies observed for the HCl elimination channel could result from the substantial exit barrier on the ground-state potential energy surface, if the dynamics for that channel proceed via internal conversion to the ground state.

The low-kinetic-energy Cl peak contributes ~5% of the total C−Cl bond fission of C_3H_3Cl at 193 nm, depending somewhat on how the background is subtracted. Two possible explanations for this peak deserve consideration. The first is that this peak is produced by decomposition on the surface of a lower-lying singlet or triplet state, which is populated by internal conversion or intersystem crossing from the initially prepared level. This lower-lying level could very well be the electronic ground state. Such a dissociation process is expected to be relatively slow, which is consistent with the isotropic product angular distribution for the low-energy Cl peak; however, in this system, the high-recoil-kinetic-energy peak is also isotropic, so the anisotropy does not provide support for this assignment of the dissociation mechanism. A similar low-kinetic-energy component has been observed in the C−X bond fission of many related alkenyl halides. In particular, the 193-nm photodissociation of 2-chloropropene[7] and vinyl chloride result in both high- and low-recoil-kinetic-energy C−Cl fission channels, and the low-recoil-kinetic-energy channel has been attributed to dissociation on the ground-state surface. However, recent work on the 193-nm photodissociation of 2-chloro-2-butene[6] suggests the corresponding low-kinetic-energy C−Cl bond fission channel does not produce ground-electronic state radicals. In this case, the radicals' subsequent C−C bond fission dynamics was very different than that of the ground-state radicals identified by the momentum match to the high-kinetic-energy Cl atoms. This suggests an alternate assignment of the low-kinetic-energy C−Cl fission channel discussed below.

A second explanation for the slow Cl peak is that it results from photodissociation producing Cl atoms in conjunction with C_3H_3 in an electronically excited state. Using a theoretical C−Cl bond energy of 70 kcal/mol,[35] the maximum available energy for internal excitation of the products is 78 kcal/mol. The maximum observed translational energy in the low-kinetic-energy channel is ~18 kcal/mol, which corresponds to an internal excitation of ~60 kcal/mol in the C_3H_3 photofragment. Although there is little information available on the electronically excited states of C_3H_3,[35−41] a recent theoretical study[41]

provides a relatively comprehensive picture of the isomers and low-lying excited states of C_3H_3. Interestingly, the $1^2A''$ state with C_s symmetry is calculated to lie 57.1 kcal/mol above the C_{2v} $^2B_1$ ground state of the propargyl radical. This position is certainly consistent with the minimum amount of internal energy of the radical produced in the low-recoil-kinetic-energy C−Cl fission channel here. Confirmation of either dissociation mechanism must await additional experiments and theoretical analysis.

IV. Conclusions

The principal conclusions are (1) the Cl ($^2P_{3/2}$) and Cl* ($^2P_{1/2}$) branching fractions in the C−Cl bond fission are 0.50 ± 0.1 and 0.50 ± 0.1, respectively; and (2) the slow Cl peak observed here and in the earlier studies[8−10] does not result from cracking of HCl in the electron-impact ionization process. Rather, it is associated with C−Cl bond fission to produce Cl ($^2P_{3/2}$), either following internal conversion to the ground electronic surface or possibly in association with electronically excited C_3H_3 radicals. Consideration of momentum matching requirements, along with comparison with the Cl, Cl*, and C_3H_3 $P(E_T)$ distributions obtained from the imaging data, indicates that the time-of-flight data obtained at $m/e = 36$ can be primarily associated with HCl elimination; the data give limits on how much of this signal may be attributed to C_3H_3 dissociatively ionizing to C_3^+. Finally, it is noted that, although secondary decomposition of the vinyl radical coproduct has been observed following the 193-nm photodissociation of vinyl chloride (C_2H_3Cl),[3] secondary decomposition via H-atom loss is energetically inaccessible for propargyl radicals produced in the 193-nm photodissociation of propargyl chloride.

Although it is clear from the present discussion that no one technique can provide all the answers, the combination of techniques described here clarifies several issues arising in previous studies and provides a reasonably consistent picture of the photodissociation dynamics of propargyl chloride. Nevertheless, independent determinations of the Cl:Cl* branching fractions and the relative yields of C−Cl bond fission and HCl elimination would provide valuable confirmation of the present analysis.

Acknowledgment. We would like to thank the GAM Laser Company for the loan of an excimer laser during the course of this work. We would also like to thank Maria Krisch and Marie Justine Bell for help setting up this laser at the University of Chicago. D.B. acknowledges the Beckman Scholars program at the University of Chicago and the Arnold and Mebel Beckman Foundation. Work at Argonne was supported by the U.S. Department of Energy, Office of Science, Office of Basic Energy Sciences, Division of Chemical Sciences, Geosciences, and Biosciences (under Contract No. W-31-109-Eng-38). Work at the University of Chicago was supported by the U.S. Department of Energy, Office of Science, Office of Basic Energy Sciences, Division of Chemical Sciences, Geosciences, and Biosciences (under Grant No. DE-FG02-92ER14305).

References and Notes

(1) Riley, S. J.; Wilson, K. R. *Faraday Discuss. Chem. Soc.* **1972**, *53*, 132.

(2) Schinke, R. *Photodissociation Dynamics*; Cambridge University Press: New York, 1993.

(3) Blank, D. A.; Sun, W.; Suits, A. G.; Lee, Y. T.; North, S. W.; Hall, G. E. *J. Chem. Phys.* **1998**, *108*, 5414.

(4) Mueller, J. A.; Parsons, B. F.; Butler, L. J.; Qi, F.; Sorkhabi, O.; Suits, A. G. *J. Chem. Phys.* **2001**, *114*, 4504.

(5) Browning, P. W.; Kitchen, D. C.; Arendt, M. F.; Butler, L. J. *J. Phys. Chem.* **1996**, *100*, 7765.

(6) McCunn, L. R.; Krisch, M. J.; Liu. Y.; Butler, L. J.; Shu, J. *J. Phys. Chem. A* **2005** *109*, 6430.

(7) Parsons, B. F.; Butler, L. J.; Ruscic, B. *Mol. Phys.* **2002**, *100*, 865.

(8) Kawasaki, M.; Kasatani, K.; Sato, H.; Shinohara, H.; Nishi, N. *Chem. Phys.* **1984**, *88*, 135.

(9) Lee, Y.-R.; Lin, S.-W. *J. Chem. Phys.* **1998**, *108*, 134.

(10) Robinson, J. C.; Sveum, N. E.; Neumark, D. M. *J. Chem. Phys.* **2003**, *119*, 5311.

(11) Harper, S.; Calandra, P.; Price, S. D. *Phys. Chem. Chem. Phys.* **2001**, *3*, 741.

(12) Morter, C. L.; Farhat, S. K.; Adamson, J. D.; Glass, G. P.; Curl, R. F. *J. Phys. Chem.* **1994**, *98*, 7029.

(13) Tonokura, K.; Matsumi, Y.; Kawasaki, M.; Tasaki, S.; Bersohn, R. *J. Chem. Phys.* **1992**, *97*, 8210.

(14) Liyanage, R.; Yang, Y.; Hashimoto, S.; Gordon, R. J.; Field, R. W. *J. Chem. Phys.* **1995**, *103*, 6811.

(15) Skorokhodov, V.; Sato, Y.; Suto, K.; Matsumi, Y.; Kawasaki, M. *J. Phys. Chem.* **1996**, *100*, 12321.

(16) Cao, J.; Loock, H. P.; Qian, C. X. W. *Can. J. Chem.* **1994**, *72*, 758.

(17) Zhang, J.; Dulligan, M.; Wittig, C. *J. Chem. Phys.* **1997**, *107*, 1403.

(18) Ahmed, M.; Blunt, D.; Chen, D.; Suits, A. G. *J. Chem. Phys.* **1997**, *106*, 7617.

(19) Liu, Y.; Butler, L. J. *J. Chem. Phys.* **2004**, *121*, 11016.

(20) Eppink, A. T. J. B.; Parker, D. H. *Rev. Sci. Instrum.* **1997**, *68*, 3477.

(21) Aguirre, F.; Pratt, S. T. *J. Chem. Phys.* **2003**, *118*, 1175.

(22) Fan, H.; Pratt, S. T. *J. Chem. Phys.* **2005**, *123*, 204301.

(23) Dribinski, V.; Ossadtchi, A.; Mandelshtam, V. A.; Reisler, H. *Rev. Sci. Instrum.* **2002**, *73*, 2634.

(24) Person, M. D. Ph.D. Thesis, University of Chicago, Chicago, IL, 1991.

(25) Moore, C. E. *Atomic Energy Levels, Vol. I*; NSRDS−NBS 35; National Bureau of Standards: Washington, DC, 1971.

(26) Zare, R. N. *Mol. Photochem.* **1972**, *4*, 1.

(27) Samartzis, P. C.; Bakker, B. L. G.; Rakitis, T. P.; Parker, D. H.; Kitsopoulos, T. N. *J. Chem. Phys.* **1999**, *110*, 3351.

(28) Neyer, D. W.; Heck, A. J. R.; Chandler, D. W.; Teule, J. M.; Janssen, M. H. M. *J. Phys. Chem. A* **1999**, *103*, 10388.

(29) Kummel, A. C.; Sitz, G. O.; Zare, R. N. *J. Chem. Phys.* **1986**, *85*, 6874.

(30) Bonin, K. D.; McIlrath, T. J. *J. Opt. Soc. Am. B* **1984** *1*, 52.

(31) Melikechi, N.; Allen, L. *J. Opt. Soc. Am. B* **1986** *3*, 41.

(32) Center, R. E.; Mandl, A. *J. Chem. Phys.* **1972** *57*, 4104.

(33) Miller, T. M.; Bederson, B. *Adv. At. Mol. Phys.* **1977** *13*, 1.

(34) See, for example, the branching ratio determinations for the photodissociation of methyl iodide and methyl bromide in, respectively: van Veen, G. N. A.; Baller, T.; de Vries, A. E.; van Veen, N. J. A. *Chem. Phys.* **1984**, *87*, 405, and van Veen, G. N. A.; Baller, T.; de Vries, A. E. *Chem. Phys.* **1985**, *92*, 59. The I/I* branching ratio determined from the electron impact CH_3^+ data in that work and the electron impact I^+ data are the same, showing that high-energy electron bombardment ionization does not preferentially detect halogen atoms in the X $^2P_{1/2}$ state over halogen atoms in the spin−orbit ground state.

(35) Atkinson, D. B.; Hudgens, J. W. *J. Phys. Chem. A* **1999**, *103*, 7978.

(36) Fahr, A.; Hassanzadeh, P.; Laszlo, B.; Huie, R. E. *Chem. Phys.* **1997**, *215*, 59.

(37) Giri, B. R.; Hippler, H.; Olzmann, M.; Unterreiner, A. N. *Phys. Chem. Chem. Phys.* **2003**, *5*, 4641.

(38) Atkinson, D. B.; Hudgens, J. W. *J. Phys. Chem. A* **1999**, *103*, 4242.

(39) Honjou, H.; Yoshimine, M.; Pacansky, J. *J. Phys. Chem.* **1987**, *91*, 4455.

(40) Botschwina, P.; Oswald, R.; Flügge, J.; Horn, M. *Z. Phys. Chem.* **1995**, *188*, 29.

(41) Nguyen, T. L.; Mebel, A. M.; Kaiser, R. I. *J. Phys. Chem. A* **2001**, *105*, 3284.